

## Rapid Electrochemical Synthesis of Hydrogenated Graphene Oxide Using Ni Nanoparticles

Rahul Krishna<sup>1</sup>, Elby Titus<sup>1,\*</sup>, Olena Okhay<sup>1</sup>, João Campos Gil<sup>2</sup>, João Ventura<sup>3</sup>, E. Venkata Ramana<sup>4</sup>, José J. A. Gracio<sup>1</sup>

<sup>1</sup>Nanotechnology Research Division (NRD), Centre for Mechanical Technology and Automation (TEMA), Dept. of Mechanical Engineering, University of Aveiro, 3810-193, Portugal

<sup>2</sup>Department of Physics, University of Coimbra, Coimbra, P-3004 516, Portugal

<sup>3</sup>IFIMUP-IN and Faculty of sciences, University of Porto, 4169-007 Porto, Portugal

<sup>4</sup>I3N, Department of Physics, University of Aveiro, 3810-193 Aveiro, Portugal

\*E-mail: [elby@ua.pt](mailto:elby@ua.pt)

*Received:* 30 October 2013 / *Accepted:* 3 December 2013 / *Published:* 14 April 2014

---

A novel method for the rapid hydrogenation of graphene oxide (GO) is established using nickel nanoparticles (Ni NPs) and through electrochemical reaction. In-situ generated hydrogen and enhanced spillover on graphene sheet makes the hydrogenated graphene oxide (HGO) easily at room temperature. Initially, a well intercalated Ni-GO species was produced due to the nanosize effect of nickel nanoparticles and promoted the homogenous hydrogenation of GO sheets. The structure, composition and morphology of GO, Ni-GO and HGO were fully characterized. I-V characteristics of HGO showed very interesting properties such as hysteresis, resistive switching and rectifier properties.

---

**Keywords:** Graphene oxide, nickel nanoparticles, hydrogenation, resistive switching, current rectification

### 1. INTRODUCTION

Excitement surrounds the discovery of graphene due to its extensive potential as novel material for large number of applications [1-4]. As a truly two dimensional (2D) system graphene possess unique electronic properties compared to conventional semiconductors [5]. In order to explore their remarkable properties in nanoelectronics, it would be highly desirable to obtain nonlinear I-V characteristics [6-7].

Hydrogenation of graphene is an efficient way for tuning the electrical behaviour of graphene and such hydrogenated graphene (HG) can deploys wide usability for various low power electronics applications [8]. Examples include supercapacitor, Li-ion batteries, spintronic devices, resistive

switching, rectifier and memristive components [9-14]. Similarly it can also find application in hydrogen storage within the graphene sheet [15]. In this contest, enormous efforts are going on for conversion of  $sp^2$  to  $sp^3$  hybridization and formation of saturated C-H bonding [16].

Exfoliation of graphite into graphene oxide (GO) is more interesting due to the low cost, high yield and easy processibility of graphene [17]. However, GO possess various kinds of oxygen functionalities and are reducible by numerous methodology [18]. Using metallic bulk powder (Mg, Al, Fe and Zn) in the presence of strong acidic medium ( $M/H^+$ ) is an attractive method for GO reduction [19-21]. But, in this series another transition metal Ni behaves differently probably due to its specific electronic configuration [Ar,  $3d^8, 4s^2$ ] and low redox potential ( $E^0 = -0.28V$ ) [22]. It does not directly reduces the GO to reduced graphene oxide (RGO), instead it makes the hydrogenated product through spillover mechanism [23].

However, its low reactivity (slow dissolution in acidic medium and agglomeration of bulk counterpart) hinders the wide applicability for hydrogenation of GO. To solve such kind of problem first time we are reporting the usability of Ni nanoparticles (Ni size~10-25 nm) for making the hydrogenated graphene oxide (HGO). Moreover, due to the nano-size effect particles are well dispersed on graphene sheet the whole synthesis was accomplished only in 3 h. Also, we have analyzed the electrical properties of HGO, showed the switching, hysteresis and rectifier properties.

## 2. EXPERIMENTAL

### 2.1 Raw Materials

Natural flake graphite (particle size 100 mesh),  $KMnO_4$ ,  $H_2SO_4$  (95-98%),  $NaNO_3$ ,  $H_2O_2$  (30% v/v), Zinc bulk powder and Conc. HCl (36.5-38%) were purchased from Sigma-Aldrich Co. Nickel nanoparticles (Av. particle size ~ 15 nm) were purchased from Quantum sphere. All chemicals were of analytical grade and all aqueous solutions were prepared with deionised distilled (DD) water ( $>18.2M\Omega.cm$ ) from a Milli-Q Plus system (Millipore).

### 2.2 Synthesis of GO

Graphene oxide (GO) was synthesized by modified Hummer's method [22-23]. Briefly, graphite flakes (1g) were dispersed in Conc.  $H_2SO_4$  (46 ml) by magnetic stirring (45 min) at low temperature ( $0-5^\circ C$ ). Later,  $NaNO_3$  (500 mg) and  $KMnO_4$  (6 g) were slowly mixed in acidic solution and continuously stirred for 2h and the temperature was increased to  $35^\circ C$ . Followed by, 10 ml, 30% v/v  $H_2O_2$  was slowly poured into the solution for further promoting the oxidation of graphite. Finally, DD water (230 ml) was added into the solution and the suspension was heated up to  $98^\circ C$  for 30 min. After completion of reaction, resultant suspension was centrifuged (3000 rpm) in order to remove the residual unexfoliated graphite and subsequently filtered and washed with DD water and dilute HCl (until the pH of the filtrate was neutral) for removing remaining impurities and oxidizing agents. Finally, GO slurry was freeze-dried and stored in a vacuum oven at RT.

### 2.3 Synthesis of HGO

Hydrogenated graphene oxide (HGO) was synthesized by electrochemical hydrogenation of GO. In this reaction H<sub>2</sub> gas was *in-situ* generated by electrochemical reaction of Ni NPs and HCl (Ni/H<sup>+</sup>) for full detail see mechanism section 3.6.

### 2.4 Characterization

Phase purity and crystallinity of GO, intermediate Ni-GO and final product HGO were analysed by X-ray diffraction (XRD) technique (Rigaku, Japan, CuK<sub>α</sub> radiation; 2θ angle range 5–80°; step 0.02°/s). UV-vis spectra of GO, HGO and RGO were collected by Shimadzu UV-2501PC (UV-vis) spectrophotometer in the absorbance mode. FTIR spectra of GO and HGO were recorded using a KBr pallet method. The Raman spectra of GO and HGO were obtained at room temperature in back scattering configuration with a Jobin-Yvon Lab Ram HR using 532 nm HeCd laser line. The morphology of GO, intermediate Ni-GO and final product HGO was investigated by scanning electron microscope (SEM) and conventional high-resolution (HR) TEM (Phillips-LaB6 TEM). The samples for TEM were prepared by dipping an aliquot of suspension (in ethanol, 0.2 mg/ ml) on to a carbon-coated copper grid. For electrical measurements, GO and HGO films (1mg/ ml in isopropanol) were prepared on Si/SiO<sub>2</sub> substrate by drop coating. GO sample was dried at RT. HGO samples were prepared in two sets, one was dried at 50°C for 2h and another was heat treated at 150°C for 6h (annealed) sample in vacuum oven. Current vs. Voltage (I-V) curve were recorded using two probe Keithley electrometer (model 2410-C) at RT.

## 3. RESULTS AND DISCUSSION

### 3.1. XRD of GO, intermediate species Ni-GO and HGO

Fig.1 shows the XRD patterns of GO, intermediate species Ni-GO and HGO samples. GO exhibits a sharp peak at around 9.09° corresponding to the (001) basal plane with d spacing of (d<sub>001</sub> = 0.961nm). This value was higher than the interlayer spacing of graphite flakes (d-spacing= 0.334nm, 2θ =26.4°), due to the presence of oxygenated functional groups and intercalated water molecules [21, 23]. After the intercalation of Ni NPs with GO three additional peaks (1 1 1), (2 0 0) and (2 2 0) were observed in intermediate species Ni-GO that were related to the various crystallographic planes of face-centred cubic (fcc) Ni-NPs [JCPDS card No. 04-0850] and the highest intense diffraction peak at around 44.4° suggest the crystallinity of Ni-NPs [24].

In HGO all these three additional peaks were eliminated and only one peak was observed with small shift at 10.9° indicates hydrogenation of GO (in presence of Ni NPs) was more significant compared to the restoration of graphitic domains. However, normal reduction profile suggests the formation of RGO by XRD peak shifting towards characteristic graphitic peak position, either using of hydrazine hydrate or other kind of reducing metal species like (Mg, Al, Fe and Zn) in acidic medium [19-21].

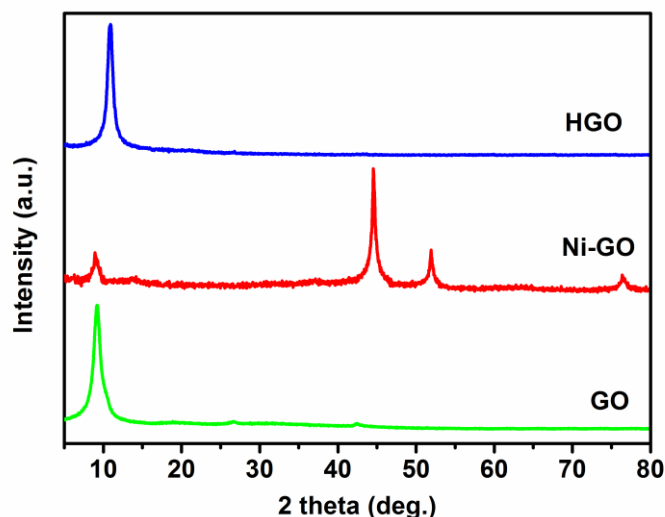


**Figure 1.** XRD pattern of the GO, Ni-GO and HGO.

### 3.2. UV-vis spectra of GO, HGO and RGO (Zn/HCl for comparison)

Further we have performed the UV-vis absorption spectra of GO, HGO and RGO (GO reduced by Zn/HCl in same reaction condition, for comparison to investigate the recovery of conjugative C=C bonding). Fig.2 shows that GO possess two characteristic absorption bands at 230 nm and 300 nm (assigned as in shoulder form). These bands were related to the  $\pi \rightarrow \pi^*$  aromatic (C=C) and  $n \rightarrow \pi^*$  (C=O) transitions, respectively [20, 21, 23]. While in HGO a broad band was observed in the range of 250-280 nm suggests the some reduction of carbonyl functionalities and enrichment of (-C-H) saturated bonds. Whereas, spectra of RGO shows clear distinction from GO and HGO, depicts a strong sharp peak at around 267 nm suggests almost removal of oxygen functionality and establishment of C=C conjugated graphene structure.

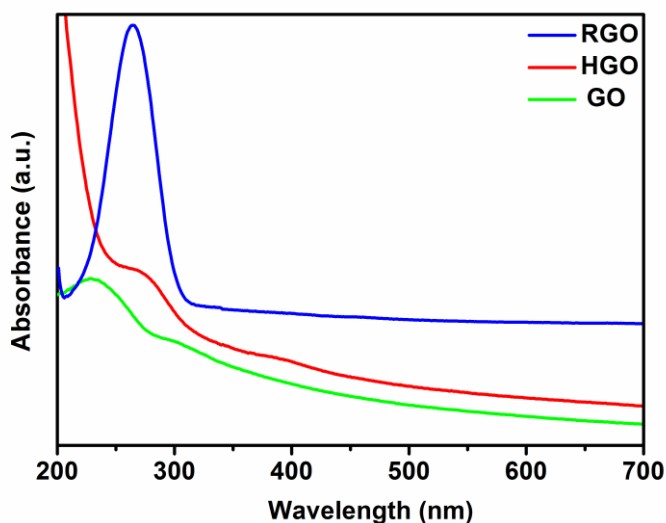


**Figure 2.** UV-vis. spectra of the GO, HGO and RGO.

### 3.3. FTIR spectra of GO and HGO samples

In order to elucidate the structure of HGO and reaction mechanism in more detail, we have also carried out the Fourier transform infrared (FTIR) spectroscopy. Fig.3 shows the FTIR spectra of GO and HGO samples (in the range of 2500-3000  $\text{cm}^{-1}$ ). In HGO, two sharp peaks were observed at around 2853 and 2923  $\text{cm}^{-1}$  and both were attributed as corresponding symmetric and asymmetric C-H stretching mode of  $\text{sp}^3\text{-C}$  ( $\nu_{\text{C-H}}$ ) vibrations [23]. The evolution of these two peaks in HGO (with distinction of GO) directly infers the hydrogenation of GO.

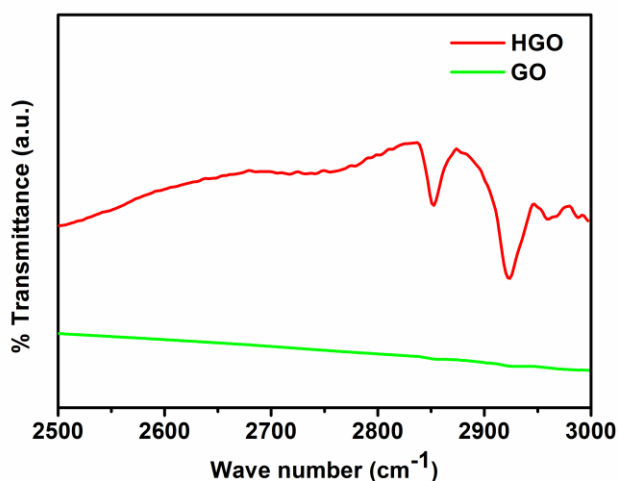


**Figure 3.** FTIR spectra of the GO and HGO.

### 3.4 Raman spectra of GO and HGO samples

Further, to ascertain the successful hydrogenation of GO and HGO, Raman spectroscopy was used. This technique is very useful for assigning the corresponding changes of graphene material on the basis of peak position and intensity. Fig. 4 (a) shows the Raman spectrum of GO and HGO in the range of 1000-1800  $\text{cm}^{-1}$ .

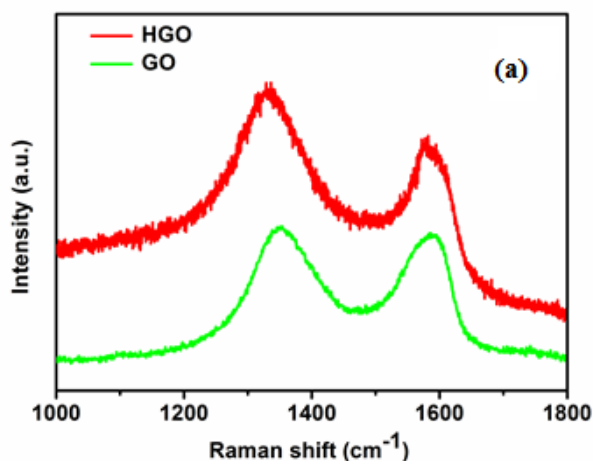


**Figure 4a.** Raman spectra of the GO and HGO.

In GO spectra two prominent bands D and G were located at  $1349\text{ cm}^{-1}$  at  $1588\text{ cm}^{-1}$  with respective  $I_D/I_G$  ratio of 0.98. This is well known fact that G band is an intrinsic feature of graphitic system and it corresponds to the first-order scattering of the  $E_{2g}$  mode of  $sp^2$  domain of carbon (related to the all  $sp^2$  carbon vibrations in long-wavelength optical phonons TO and LO) [25-27]. D band is arising after the defect introduction and related to the characteristic breathing mode of  $A_{1g}$  symmetry [28]. Whereas in HGO, both D and G bands were shifted to lower wave number (red-shifted) and appeared at  $1333$  and  $1584\text{ cm}^{-1}$ , respectively with increased  $I_D/I_G$  ratio of  $\sim 1.36$ . This increment of  $I_D/I_G$  ratio in HGO provides a clear evidence for corresponding changes inside carbon system after the reduction. Moreover, asymmetric shape and broadening of G band in HGO also suggests the possible hydrogenation of carbon system. Fig. 4 (b) shows that the Laurentian peak fitted data of HGO and after the deconvolution of G band, two peaks were clearly observed and higher wave number peak around at  $\sim 1608\text{ cm}^{-1}$  represents the D' defect band [29]. This was already reported that D' band is related to nonzero phonon density of states above the G band and become active after the defect introduction or double resonance process [30-31].

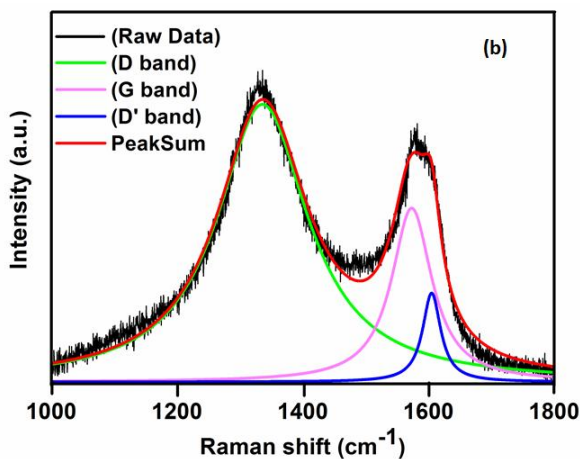
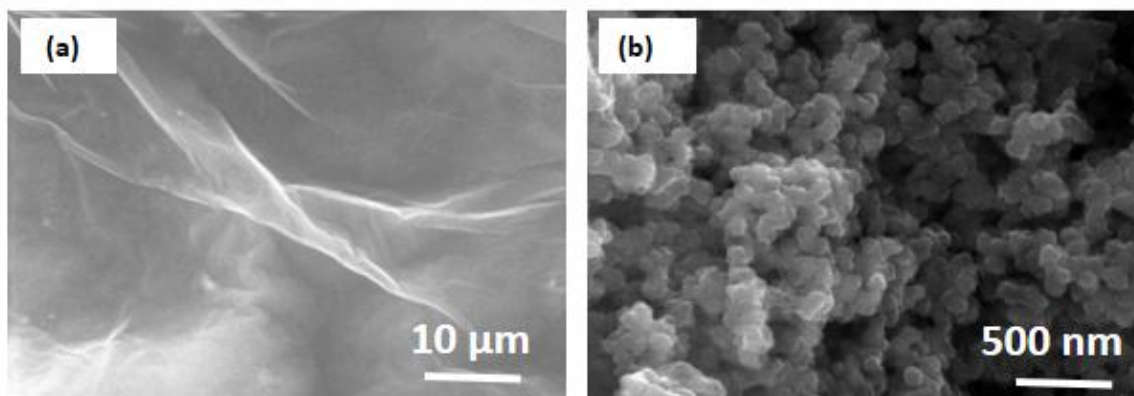


**Figure 4b.** Fitted Raman spectra of HGO after deconvolution of D and G band.

In our case we are assuming the Raman scattering near to the “intra-valley” by the promotion of ‘out-of-plane’ ripple induced  $sp^3$  hybridization (-C-H bonding) mediated by phonons nearby  $\Gamma$  and K (or K') points [32]. A recent Monte Carlo simulation study also supports the  $sp^3$  (-C-H) bonding is favourable in rippled graphene than that of flat graphene [33]. To confirm this, we have also performed the microscopic analysis to investigate the morphology and microstructure of our product.

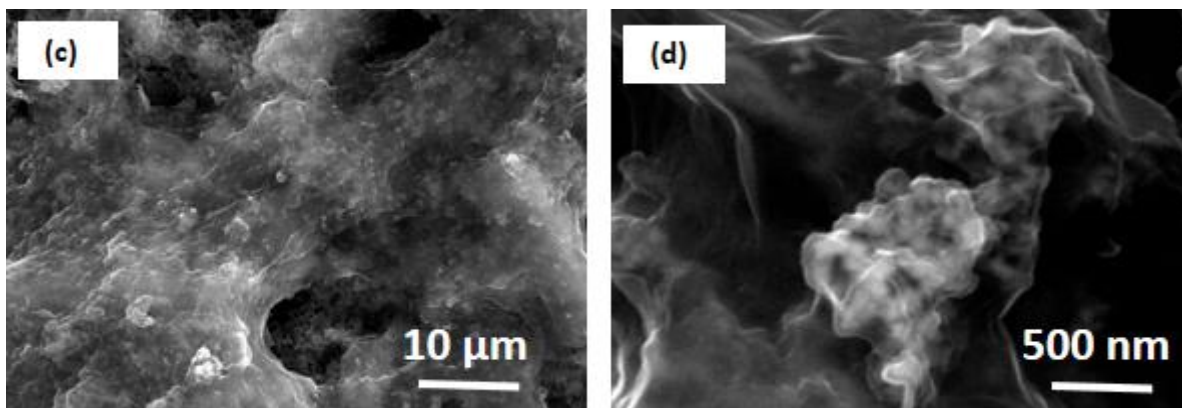
### 3.5 Microscopic (SEM and TEM) analysis of GO, Ni nanoparticles, Ni-GO and HGO sample

We have carried out systematic microscopic investigation of initial materials (GO and Ni NPs), intermediate composite material Ni-GO (after the loading of Ni NPs within the GO matrix) and final product HGO.



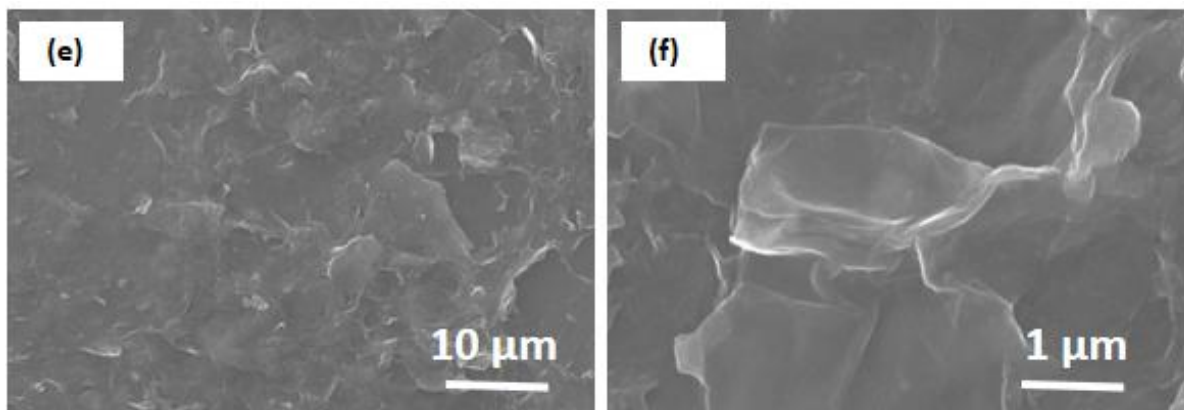
**Figure 5.** (a) and (b) SEM images of initial material GO and Ni nanoparticles.

Fig.5(a) and (b) shows the SEM images of GO and Ni nanoparticles, respectively. Image of GO clearly exhibits the few layer of graphitic carbon with typical wrinkle behaviour [19-21]. Image (b) displays the initial morphology and size of the Ni NPs and shows that all particles were in nano regime with spherical shape. Fig. 5 (c & d) shows the SEM images of intermediate species Ni-GO after the loading of Ni NPs with GO. Both the images depicts well intercalation of Ni NPs with graphitic flakes and image contrast in higher magnification image (white spots on black background) clearly reveals the covering of Ni NPs by single or few layers graphene sheets.



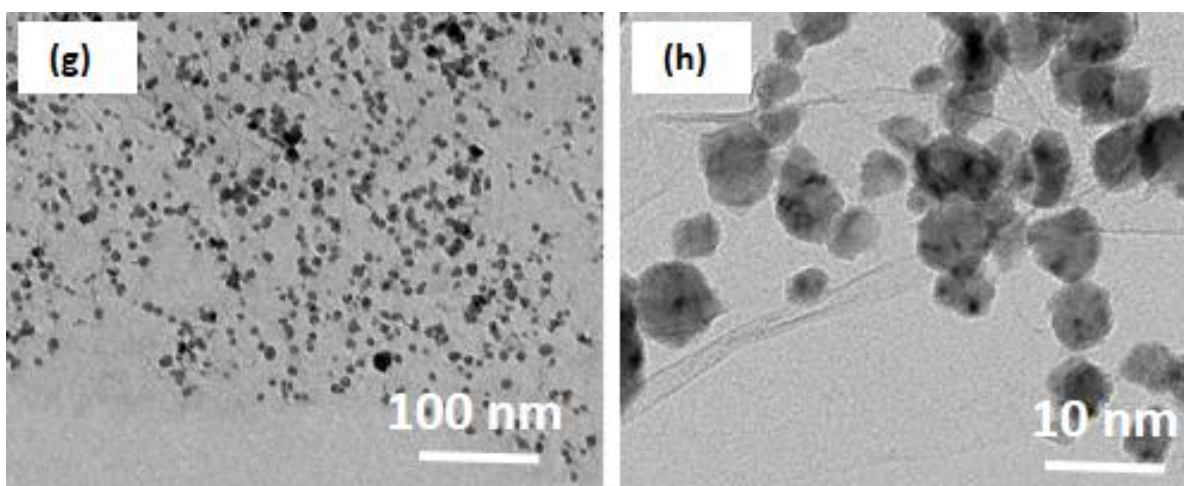
**Figure 5.** (c) and (d) SEM images of intermediate Ni-GO composite material in lower and higher magnification.

Fig. 5 (e&f) displays the lower and higher magnifications SEM images of HGO after the reduction and apparently there was no particles were observed. The absence of Ni NPs was obvious because during the reduction process Ni NPs were oxidized by conc. HCl and produces the cations that were removed after washing. Interestingly, in HGO carbon sheet was less agglomerated as compared to Ni-GO and GO. This can be explained as: during the reduction process internal hydrogen bonding of carbon system related to carboxylic and carbonyl ( $-C=O$ ) group of GO disrupted and these polar functionalities  $sp^2$  may be transformed in to the  $sp^3$  ( $-C-H$ ) moiety and later species is less polar which pursues the weak interaction between graphene sheet.



**Figure 5.** (e) and (f) SEM images of final product HGO in lower and higher magnification.

Further, we have performed the TEM analysis of intermediate Ni-GO and HGO for detailed investigation of morphology and internal structure. Fig. 5 (g&h) shows the lower and higher magnification TEM images of Ni-GO. Here, we clearly visualized the Ni NPs homogeneously distributed on graphene sheet and higher magnification image shows that the all particles were less than 20 nm and in spherical shape without any kind of specific change in morphology.



**Figure 5.** (g) and (h) TEM images of intermediate Ni-GO in lower and higher magnification.

Fig. 5 (i&j) shows the TEM images of final product HGO and in low magnification, typical crumpled and wrinkled behaviour of carbon sheet with single to few layer of graphene was observed. Further, we have performed the selective area electron diffraction (SAED) analysis of HGO and observed the distortion in hexagonal carbon network (inset image of Fig. 5i). This can be explained as, after the hydrogenation, oxygen functionalities and graphitic domains get saturated and led to the formulation of  $sp^3$  (-C-H) structure. However, initial experimental work related to hydrogenation of graphene (graphane synthesis) reflects the equidistance position of diffraction spots [15].

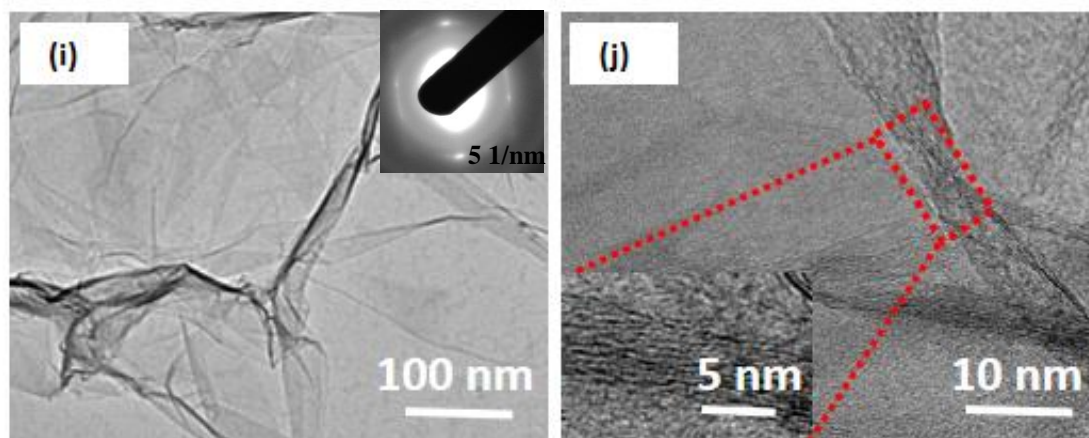
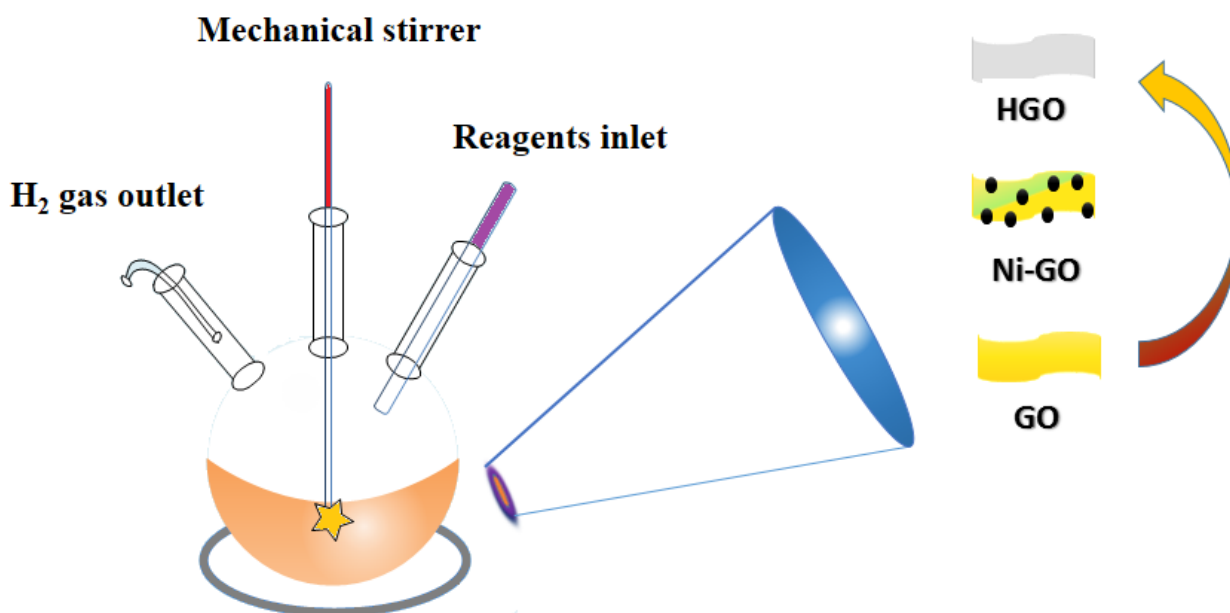


**Figure 5.** (i) and (j) TEM images of final product HGO in lower and higher magnification. The corresponding inset image of Fig 5 (i) is SAED and Fig. 5 (j) 4X magnified area.

This was probably due to the hydrogenation of consistent hexagonally arranged initial material (graphene) which pertains the  $sp^2$  hybridized regular hexagonal ring structure. However, SAED of HGO is entirely different from the original GO and graphene [15-16, 19-21]. Further, deformation in carbon system was also clear at higher magnification (inset of Fig. 5j) which also shows the less regularization of graphene sheet.

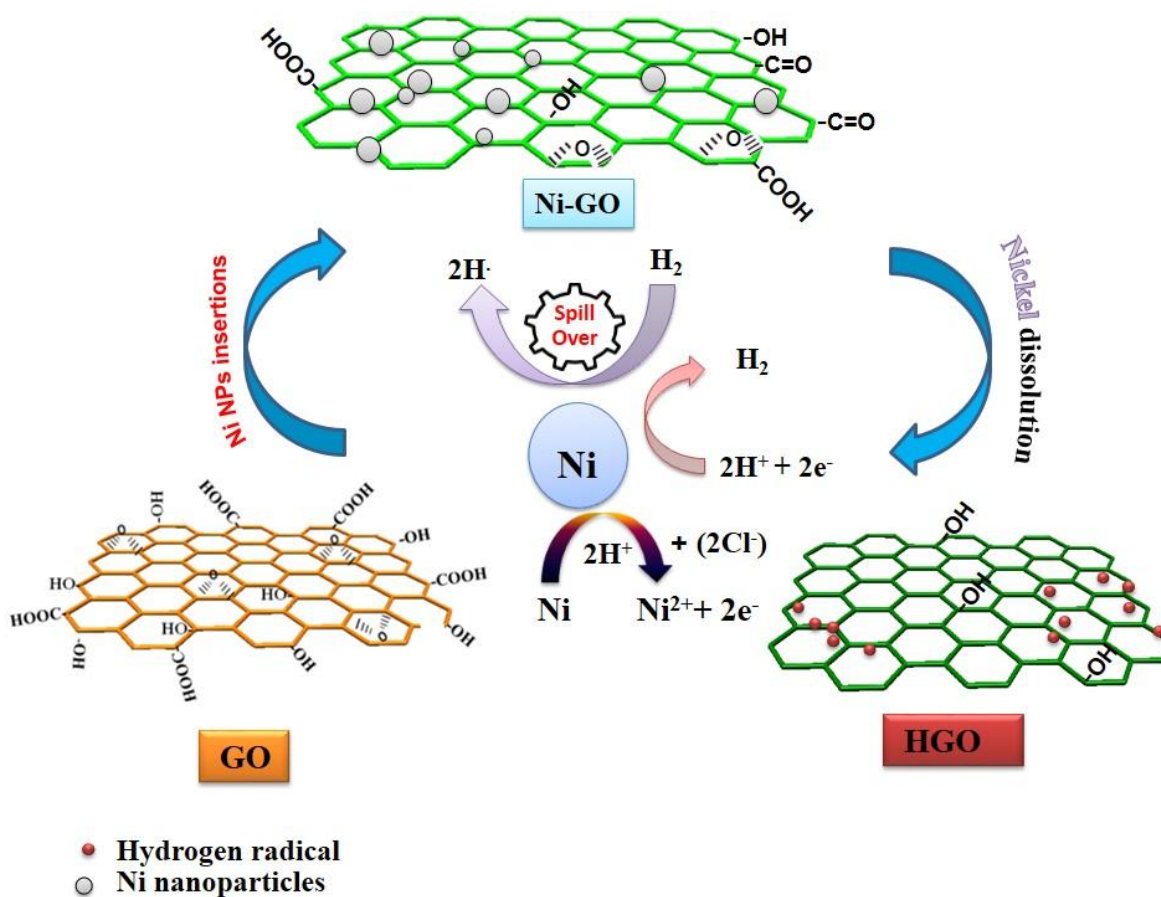
### 3.6 Mechanism of HGO formation



**Scheme 1.** Instrumental setup and representation of HGO synthesis.

Scheme 1 illustrates the instrumental representation for the synthesis of HGO. For this 30 ml well dispersed GO suspension (2mg/ml) was poured in 250 ml round bottom (RB) flask. Followed by, a pre-calculated amount of Ni NPs (300 mg) were dispersed in GO suspension for 15 min

ultrasonication at RT and this homogenised suspension is referred as Ni-GO intermediate species. Further, 39 ml of conc. HCl was added in above suspension in three equal parts (13 ml each, with a time interval of 45 min) and suspension was continuously stirred by teflon coated mechanical stirrer for 3h. To ensure the maximum hydrogenation of GO by *in-situ* generated  $H_2$ , the reaction was carried out at RT (25 °C) and acid was slowly poured during the reaction. The whole reaction was accomplished in well ventilated fume hood with temperature controller. After the completion of reaction, top part of the product (HGO) was precisely collected and bottom part of the solution was discarded to remove the unreacted metallic impurities. Finally, the product was 2-3 times centrifuged (4000 rpm, 10 min) to remove the cationic and anionic impurities and repeatedly washed with DD water and dried at 100°C. We interpret the mechanism as follows: as illustrated in Scheme 2 an intermediate Ni-GO was also formed during the course of reaction. Moreover, the well attachment of Ni NPs with GO provides the easiness of hydrogenation of GO and facile transformation of radical hydrogen ( $H^\cdot$ ) to the carbon skeleton. In this process, Ni NPs reacts with hydrochloric acid (aq) and produces the  $Ni^{2+}$  and  $2e^-$  through electrochemical reaction between Ni metal and acid ( $Ni + 2HCl = Ni^{2+} + 2Cl^- + 2H^+ + 2e^-$ ).



**Scheme 2.** Schematic representation of GO to HGO formation *via* intermediate species Ni-GO through continuous hydrogen spillover process during the reaction.

Further, proton and electrons combines together ( $2\text{H}^+ + 2\text{e}^- = \text{H}_2$ ) and produces the hydrogen gas [34]. In this process Ni NPs were continuously reacted with acid and reduces own size. These NPs pursuits very high catalytic activity (more smaller size tends to larger surface area and higher surface energy) and enhances spillover of hydrogen ( $\text{H}_2 = 2\text{H}^\cdot$ ) on its surfaces and makes the radical hydrogen ( $\text{H}^\cdot$ ) which is easily adsorbed onto the GO and forms the HGO ( $\text{GO} + 2\text{H}^\cdot = \text{HGO}_{\text{Red}} + \text{H}_2\text{O}$ ). GO can also be reduced by direct attachment of  $\text{H}^+$  and  $\text{e}^-$  ( $\text{GO} + m\text{H}^+ + ne^- = \text{RGO} + p\text{H}_2\text{O}$ ), but due to its low redox potential (Ni = -0.28V) it losses electrons very slowly and instead the forming of RGO makes the HGO [23]. It is already reported that the Ni is very prominent catalyst for hydrogenation of olefinic and benzene double bond and for unsaturated benzene derived carbonyl functionalities also [22-23, 34-38]. Thermodynamic stability data of hydrogenation of double bond also favours the dissociative chemisorption of hydrogen [8, 22, 34, 38]. This was already explained as: initially an adduct species is forming on catalyst surface by the breaking of  $\pi$ - $\pi$  bonding and simultaneously hydrogen molecule also dissociates in to radical hydrogen ( $\text{H}-\text{H} = 2\text{H}^\cdot$ ) making the metal hydride species (Ni-H) [8, 23].

The generated radical H migrates from Ni catalyst surface to the C-C bond through a “bridge” built and completes the process. However, in our case hydrogen molecule is generated inside the system through electrochemical reaction without any external source, further *in-situ* produced hydrogen easily spillover on own generator (nano Ni surface) and readily transforms to the unsaturated carbon sites. To describe this migration of H, here we are assuming that one Ni particles works as a (source, S) and simultaneously another nanoparticle as an (activator, Act) to dissociate the hydrogen molecule and finally the unsaturated carbon skeleton ( $-\text{C}=\text{O}$  or  $-\text{C}=\text{C}$ ) behaves as a (receptor, Rec). In this heterogeneous catalysis, the source and activator is metal (Ni) and the receptor is also semimetal (graphene) and this feature can be explained as diffusion of hydrogen inside the carbon system (C) like  $\text{S} \rightarrow \text{H}_2 \text{---} \text{Act} \rightarrow 2\text{H}, \text{H} + \text{C} \rightarrow \text{H} @ \text{C}$  [8]. Moreover, here we assume that big graphene sheet own it's on also enhances the hydrogenation process via charge polarization of  $\text{H}_2$  molecule as ( $\text{H}^{+\delta} - \text{H}^{-\delta}$ ) due to its delocalized (six membered, p- $\pi$ ) electron cloud structure.

### 3.7 I-V measurement of GO, and two sets of HGO samples

On the basis of above results, we have further performed electrical measurements on HGO with successive sweeping voltage of 1V/s step size and a delay time of 1s. Fig. 6 represents the current vs voltage (I-V) plot obtained on GO and HGO (dried at 50°C for 2h) samples in the range of -10 to +10V. It is obvious that GO is an insulator material with extremely low current values, whereas HGO shows a non-linear behaviour with an increment in current value. Moreover, HGO depicts a clear hysteresis in both sides with typical phenomenon of resistive switching material [14]. It can also be observed that, at a certain voltage (+9V) during the positive loop, the current value dramatically increased. When positive sweeping the voltage, the current changed in an anticlockwise direction, suggesting a set-like condition (SLC) or on-state that resembles a memristive behaviour (in which current switches at certain voltage range) [39]. On the other hand, at negative bias voltage a reset-like condition (RLC) or off-state was clearly observed, reflecting the same charge mobility by equivalent internal filament breakage in another side.

For better understanding, we have also performed I-V measurements in higher voltage conditions in two different ranges -15 to +15V and -20 to +20V, respectively. Fig. 7 (a) also shows the progression of the current and evolution of similar resistive switching polarity in the positive region and this systematic hysteresis suggests the polarity dependent filament rupturing inside the carbon system [40]. However, in the negative loop the situation was obscured and, instead of switching only hysteresis was retained inside the system. This was probably due to the recursion of internal  $sp^3$  (-C-H) bonding and restoration of  $sp^2$  (-C=C) graphitic structure during the process

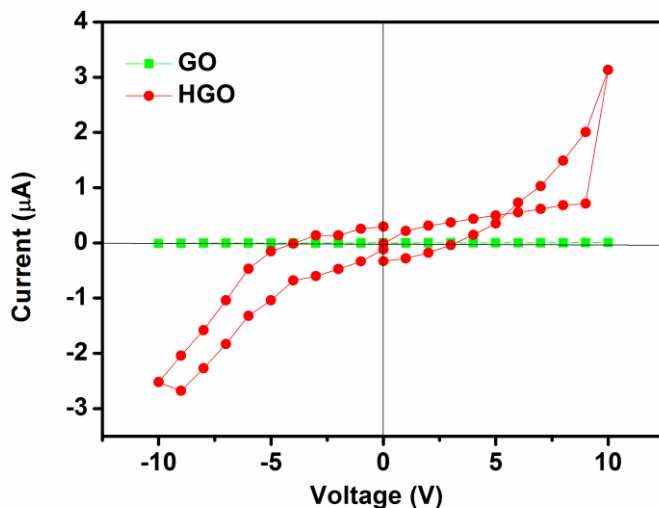


**Figure 6.** Characteristic I vs V curve of GO and HGO in bias range of (-10 to +10V). The voltage is swept in the direction as follows: 0 V → 10 V → 0 V → -10 V → 0 V.

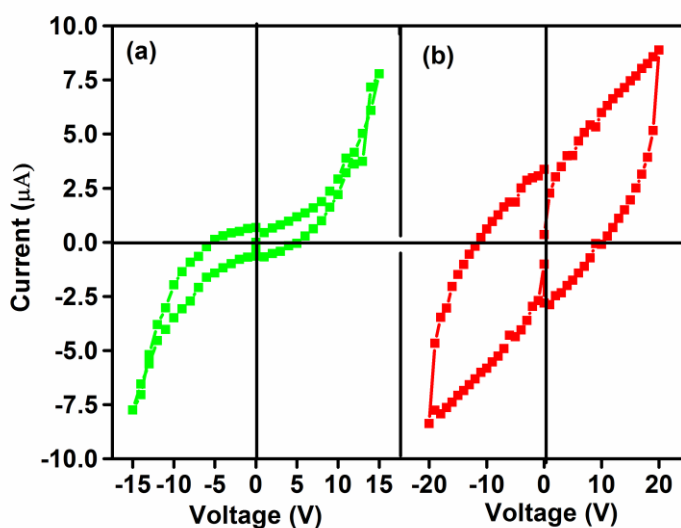


**Figure 7.** Characteristic I vs V curve of HGO in bias range of (a) sweeping voltage (-15 to +15V) and (b) sweeping voltage (-20 to +20V). The voltage is swept in the direction as follows: 0 V → 10 V → 0 V → -10 V → 0 V.

However, at higher voltage (20V), both positive and negative region represents a clear hysteresis loop without any specific switching. This was expected because, at higher voltage the whole filaments were broken and current reached the saturation and only internal charge trapping was accessible inside the system [14, 39, 41]. Furthermore, to obtain a better understanding regarding the non-linearity and temperature dependency of HGO, we have annealed the sample at 150 °C for 6h in vacuum dry oven to minimize the possibility of oxygen functionalities inside the carbon system. Fig. 8a and b depicts the I-V plot in the range of -10 to +10 V with two different scan rate. We have observed that after applying voltage, hysteresis and switching were retained inside the system but only in the positive region whereas in the negative region the situation was changed. Such phenomena can be attributed as emergence of rectifying property of HGO after the annealing process. Kim et al. reported the hydrogenation of carbon nanotube (CNT) and the rectification of current in the negative region [42]. We therefore assume that after the removal of oxygen functionalities, the remaining  $sp^3$  hybridization (-C-H) bonding is responsible for such effect. A recent theoretical work also supports the rectification property in graphene via the formulation of hybrid carbon network [43].

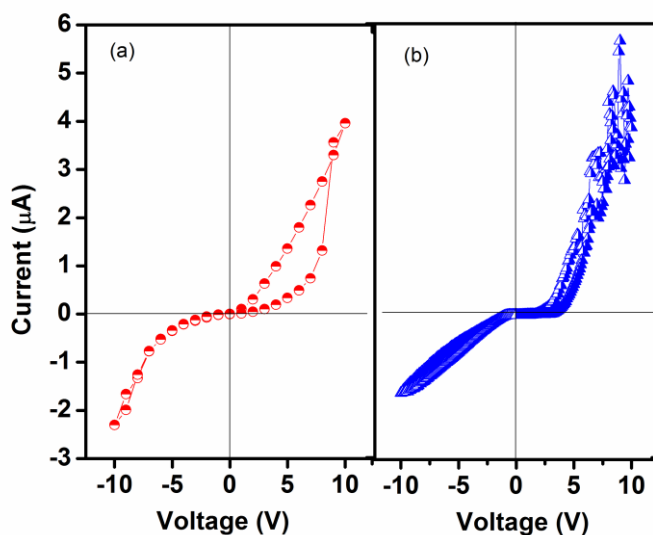


**Figure 8.** Characteristic I vs V curve of annealed sample of HGO in bias range of (-10 to +10V) with two different step sizes (a) with fast scan rate (1V/s step size) (b) with slow scan rate (0.1 V/s step size). The voltage is swept in the direction as follows: 0 V  $\rightarrow$  10 V  $\rightarrow$  0 V  $\rightarrow$  -10 V  $\rightarrow$  0 V.

Furthermore, we have performed very slow voltage scanning (0.1 V/s step size with 5s delay time for each step) in the same voltage condition to ascertain the blocking effect in the negative region. Surprisingly, in the negative region a small hysteresis was gained and in the positive side a large inconsistency in current was observed. Such behaviour clearly entails the continuous filament forming and rupturing inside the carbon system and innovatively it can be referred to as negative differential resistance (NDR) effect [44-45]. To confirm the NDR behaviour in the annealed HGO sample further we performed I-V measurement at higher voltages (-15 to +15 V and -20 to +20 V) and fast scan rates

of (1V/s with only 1 s delay time for each step) as shown in Fig. 9 (a and b). In these samples we also have observed a pronounced NDR effect in the positive bias region between 12 and 15V and 15 and 20 V respectively. These effects directly endorse the combination of rectification and NDR in annealed HGO which can also be usable for various nanoelectronics applications.

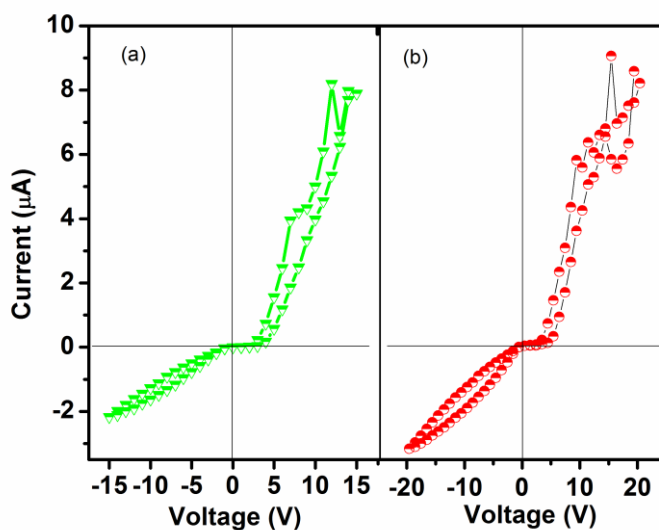


**Figure 9.** Characteristic I vs V curve of annealed sample of HGO in bias range of (a) sweeping voltage (-15 to +15V) and (b) sweeping voltage (-20 to +20V) with scan rate of (1V/s step size). The voltage is swept in the direction as follows: 0 V → 10 V → 0 V → -10 V → 0 V.

#### 4. CONCLUSIONS

In summary, HGO was synthesized at room temperature by a new approach. The quality of the HGO was characterized by various techniques. FTIR and Raman analysis clearly exhibits the successful hydrogenation of graphene sheet. A full descriptive mechanism is established for formation of HGO. I-V characteristics of HGO shows interesting results such as blocking of current, hysteresis and memristive behaviour.

#### ACKNOWLEDGEMENT

The authors gratefully acknowledge FCT Portugal (PTDC/EME- MFE/103051) and (SFRH/BD/80105/2011) for their financial support.

#### References

1. K. S. Novoselov, A. K. Geim, S. V. Morozov, D. Jiang, Y. Zhang, S. V. Dubonos, I. V. Grigorieva and A. A. Firsov, *Science*, 306 (2004) 666.
2. A. K. Geim and K. S. Novoselov, *Nat. Mater.*, 6 (2007) 183.
3. S. Park and R.S. Ruoff, *Nat. Nanotechnol.*, 4 (2009) 217.

4. D. Li, M.B. Muller, S. Gilje, R.B. Kaner, G.G. Wallace, *Nat. Nanotechnol.*, 3(2008)101.
5. K. S. Novoselov, V. I. Fal'ko, L. Colombo, P. R. Gellert, M. G. Schwab and K. Kim, *Nature*, 490 (2012) 192.
6. Y. Chen, B. Zhang, G. Liu, X. Zhuang, and E.-T. Kang, *Chem. Soc. Rev.*, 41 (2012) 4688.
7. H. Y. Jeong, J. Y. Kim, J. W. Kim, J. O. Hwang, J. E. Kim, J. Y. Lee, T. H. Yoon, B. J. Cho, S. O. Kim, R. S. Ruoff and S. Y. Choi. *Nano Lett.*, 10 (2010) 4381.
8. R. Krishna, E. Titus, M. Salimian, O. Okhay, S. Rajendran, A. Rajkumar, J. M. G. Sousa, A. L. C. Ferreira, J. C. Gil and J. Gracio, *Hydrogen Storage for energy application*, Intech Open, Europe (2012).
9. J. Yan, T. Wei, B. Shao, F. Ma, Z. Fan, M. Zhang, C. Zheng, Y. Shang, W. Qian and F. Wei, *Carbon*, 48 (2010) 1731.
10. C. Fu, G. Zhao, H. Zhang, S. Li, *Int. J. Electrochem. Sci.*, 8 (2013) 6269.
11. P. Chandrachud, B. S. Pujari, S. Haldar, B. Sanyal and D. G. Kanhere, *J. Phys.: Condens. Matter*, 22 (2010) 465502.
12. D. K. Samarakoon, R. N. Gunasinghe and X.-Q. Wang, *J. Mater. Chem. C*, 1 (2013) 2696.
13. A. Jacobsen, I. Shorubalko, L. Maag, U. Sennhauser and K. Ensslin, *Appl. Phys. Lett.*, 97 (2010) 032110.
14. S. Pinto, R. Krishna, C. Dias, G. Pimentel, G. N. P. Oliveira, J. M. Teixeira, P. Aguiar, E. Titus, J. Gracio, J. Ventura, J. P. Araujo, *Appl. Phys. Lett.*, 101 (2012) 063104.
15. D. C. Elias, R. R. Nair, T. M. G. Mohiuddin, S. V. Morozov, P. Blake, M. P. Halsall, A. C. Ferrari, D. W. Boukhvalov, M. I. Katsnelson, A. K. Geim and K. S. Novoselov, *Science*, 323 (2009) 610.
16. K. S. Subrahmanyam, P. Kumar, U. Maitra, A. Govindaraj, K. P. S. S. Hembram, U. V. Waghmare and C. N. R. Rao, *Proc. Natl. Acad. Sci. U. S. A.*, 108 (2011) 2674.
17. D. R. Dreyer, S. Park, C.W. Bielawski and R. S. Ruoff, *Chem. Soc. Rev.*, 39 (2010) 228.
18. H. Feng, R. Cheng, X. Zhao, X. Duan and J. Li, *Nature Commun.*, 4 (2013) 1927.
19. B. K. Barman, P. Mahanandia and K. K. Nanda, *RSC Adv.*, 3 (2013) 12621.
20. Z. J. Fan, W. Kai, J. Yan, T. Wei, L. J. Zhi, J. Feng, Y. M. Ren, L.P. Song, and F. Wei, *ACS Nano*, 5 (2011) 191.
21. X. Mei and J. Ouyang, *Carbon*, 49 (2011) 5389.
22. C. E. Housecroft and A. G. Sharpe, in *Inorganic Chemistry*, Pearson Prentice Hall, New Jersey (2008).
23. R. Krishna, E. Titus, L. C. Costa, J. C. J. M. D. S. Menezes, M. R. P. Correia, S. Pinto, J. Ventura, J. P. Araújo, J. A. S. Cavaleiro, J. J. A. Gracio, *J. Mater. Chem.*, 22 (2012) 10457.
24. Z. Wang, Y. Hu, W. Yang, M. Zhou and X. Hu, *Sensor*, 12 (2012) 4860.
25. F. Tuinstra and J. Koenig, *J. Chem. Phys.*, 53 (1970) 1126.
26. Y. Wang, X. Xu, J. Lu, M. Lin, Q. Bao, B. Ozyilmaz and K.P. Loh, *ACS Nano*, 4 (2010) 6146.
27. Y.Y. Wang, Z.H. Ni, T. Yu, Z.X. Shen and H.M. Wang, *J. Phys. Chem. C*, 112 (2008) 10637.
28. H. Sun, L. Cao and L. Lu, *Nano Res.*, 4 (2011) 550.
29. Z. Luo, T. Yu, Z. Ni, S. Lim, H. Hu, J. Shang, L. Liu, Z. Shen and J. Lin, *J. Phys. Chem. C*, 115 (2011) 1422.
30. Z. Luo, T. Yu, K.J. Kim, Z. Ni, Y. You, S. Lim, Z. Shen, S. Wang and J. Lin, *ACS Nano*, 3 (2009) 1781.
31. C. N. R. Rao, A. K. Sood, K. S. Subrahmanyam and A. Govindaraj, *Angew. Chem. Int. Ed.*, 48 (2009) 7752.
32. M. S. Dresselhaus, A. Jorio, A. G. Souza Filho and R. Saito, *Phil. Trans. R. Soc. A*, 368 (2010) 5355.
33. S. Ryu, M. Y. Han, J. Maultzsch, T. F. Heinz, P. Kim, M. L. Steigerwald and L. E. Brus, *Nano Lett.*, 8 (2008) 4597.
34. J. D. Lee, *Concise Inorganic Chemistry*, Oxford University press, London (2008).
35. R. T. Morrison and R. N. Boyd, *Organic Chemistry*, Wiley, New York (1993).

36. P.J. Goethe and R. T. Yang, *Journal of Catalysis*, 108 (1987) 156.
37. F. Mittendorfer and J. Hafner, *J. Phys. Chem. B* 106 (2002) 13299.
38. T. W. Solomons and C. B. Fryhle, *Organic Chemistry*, Wiley, New York (2004).
39. O. Okhay, R. Krishna, M. Salimian, E. Titus, J. Gracio, L. M. Guerra and J. Ventura, *J. Appl. Phys.*, 113 (2013) 064307.
40. J. J. Yang, D. B. Strukov and D. R. Stewart, *Nature Nanotech.*, 8 (2013) 13.
41. S. K. Hong, J. E. Kim, S. O. Kim, and B. J. Cho, *J. Appl. Phys.*, 110 (2011) 044506.
42. K. S. Kim, K. A. Park, H. J. Kim, D. J. Bae, S. C. Lim and Y. H. Lee, *J. Korean Phys. Soc.*, 42 (2003) S137.
43. Z. Zhang, J. Zhang, G. Kwong, J. Li, Z. Fan, X. Deng and G. Tang, *Scientific Reports*, 3 (2013) 1-2575.
44. M. Rinkiö, A. Johansson, V. Kotimäki and P. Törmä, *ACS Nano*, 4 (2010) 3356.
45. H. Cheraghchi and K. Esfarjani, *Phys. Rev. B*, 78 (2008) 085123.

© 2014 The Authors. Published by ESG ([www.electrochemsci.org](http://www.electrochemsci.org)). This article is an open access article distributed under the terms and conditions of the Creative Commons Attribution license (<http://creativecommons.org/licenses/by/4.0/>).